Design and Characterization of Single- and Multiple-Beam MM-Wave Circularly Polarized Substrate Lens Antennas for Wireless Communications

Xidong Wu, *Student Member, IEEE*, George V. Eleftheriades, *Member, IEEE*, and
T. Emilie van Deventer-Perkins, *Senior Member, IEEE*

Abstract—Single- and multiple-beam circularly polarized ellipsoidal substrate lenses suitable for millimeter-wave wireless communications have been designed, implemented, and experimentally characterized at 30 GHz. The lenses are made out of low-cost low-permittivity Rexolite material. The single-beam lens achieves a directivity of 25.9 dB, a front-to-back ratio of 30 dB, and an axial ratio of 0.5 dB is maintained within the main lobe. The measured impedance bandwidth is 12.5% within a $\mathrm{SWR} \leq 1.8 : 1$. The single-beam antenna is well suited for broad-band wireless point-to-point links. On the other hand, the multiple-beam lens launches 31 beams with a minimum 3-dB overlapping level among adjacent beams. The coverage of the lens antenna system has been optimized through the utilization of a hexagonal patch arrangement leading to a scan coverage of $45.4°$ with a maximum loss in directivity of 1.8 dB due to multiple reflections. The multiple-beam lens antenna is suitable for indoor point-to-multipoint wireless communications such as a broad-band local area network or as a switched beam smart antenna. During the proposed design process, some fundamental issues pertaining to substrate lens antennas are discussed and clarified. This includes the depolarization properties of the lenses, the effect of multiple internal reflections on the far-field patterns and the directivity, the nature of the far-field patterns, the estimation of the lens system F/B ratio, and the off-axis characteristics of ellipsoidal lenses.

Index Terms—Broad-band wireless communications, circular polarization, millimeter waves, multiple-beam antennas, substrate lenses.

I. INTRODUCTION

AS THE need for broad-band wireless communication systems is growing, the microwave frequency band either becomes too congested or simply cannot support the ever-increasing data-rate requirements. Therefore, the corresponding operating frequency is gradually shifting toward millimeter-wave (mm-wave) frequencies [1], [2]. In recent years, this has generated an increased interest in developing mm-wave integrated circuit (IC) antennas for indoor and outdoor wireless communications.

A successful technique for implementing mm-wave subsystems has been the integration of planar antennas and electronics at the back of substrate lenses [3]–[17]. The main advantages of this approach include highly directive antenna patterns, compatibility with IC techniques, mechanical rigidity, and thermal stability, as well as the capability of multiple-beam formation in a simple way. In addition, this approach is capable of suppressing surface-wave losses, which become an important consideration at mm-wave frequencies. The properties of hyperhemispherical and extended hemispherical lenses, such as directivity, Gaussian coupling efficiency, reflection losses, and off-axis imaging characteristics have been extensively investigated in [15]–[17]. This reported work has been based on a geometrical optics approach combined with diffraction theory to predict the far-field radiation patterns through the lens. On the other hand, the modeling of the input impedance of printed feed antennas at the back of substrate lenses has been based on the method of moments and the assumption that the lens behaves like an infinite dielectric half-space [3], [4], [16]. Recently, this work has been extended to account for second-order reflections from the lens surface on the input impedance of printed slots by means of a physical optics approach in combination with the induced electromotive force (EMF) method [5]. In addition, the design of appropriate matching layers to reduce the reflections from the lens surface have been investigated in [6].

Most of the work reported thus far has been concentrated on the fundamental properties of elementary linearly polarized slot antennas as feeds to Si or quartz lenses. These structures have been optimized for radio-astronomical, remote-sensing, or imaging applications for which specific properties such as coupling to Gaussian beams become significant. However, for wireless communication applications, other features such as circular polarization, high directivity, reduced cost, and multiple-beam formation with extended coverage become more relevant. In this paper, a realistic circularly polarized (CP) substrate lens antenna system suitable for mm-wave wireless communications is demonstrated. Both single- and multiple-beam CP substrate lens antennas operating at 30 GHz are presented. This design frequency has been selected partly due to the spectrum allocation for currently proposed mm-wave wireless systems [1], [2] and partly due to available laboratory equipment. Circular polarization and high directivity are desirable features, as they can
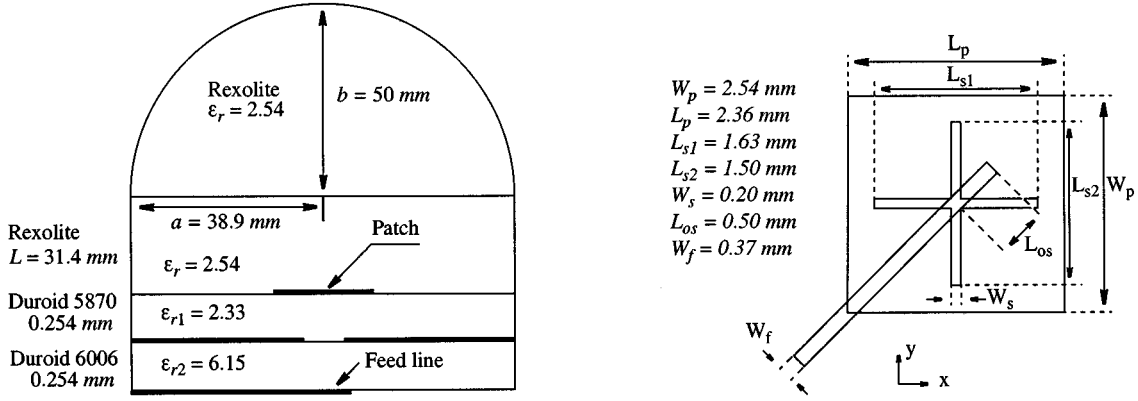
Fig. 1.   Layout for the CP single-beam ellipsoidal substrate lens.

effectively reduce multipath effects and maintain a proper link margin while conserving precious mm-wave power. In addition, multiple-beam antennas can be utilized either for point-to-multipoint links or for incorporating "smart" antenna features based on a switched beam approach in mobile applications [18].

In the above framework, a CP single-beam antenna is first introduced based on a low-cost easily machined Rexolite substrate lens. For the single-beam design, an ellipsoidal lens with a cylindrical extension slab is utilized, which leads to diffraction limited patterns on axis. The chosen feed is an aperture-coupled patch antenna, which minimizes back radiation arising from the low permittivity of Rexolite [7], [8], [14]. For the design of the multiple-beam antenna, the on- and off-axis polarization properties of Rexolite elliptical lenses with a cylindrical extension slab have been thoroughly investigated. Previously, the off-axis limitations of extended hemispherical Si or quartz lenses have been characterized based on the level of reflection losses [15]. In this paper, these off-axis properties are examined for ellipsoidal lenses and from the point-of-view of maintaining a good CP axial ratio (AR) in addition to low reflection losses. By means of this analysis, a 31-beam CP substrate lens antenna is designed and implemented based on a hexagonal arrangement of printed patch elements at the back of the lens. Supporting experimental results are presented throughout this paper.

II. ANTENNA STRUCTURE—GENERAL ANALYSIS AND DESIGN

A general schematic diagram of the single-beam substrate lens antenna is shown in Fig. 1. The lens is made out of Rexolite ($\varepsilon_r = 2.54$), a low-cost plastic material, which is easy to machine and exhibits low loss at mm-wave frequencies [20]. For generating diffraction limited patterns, an ellipsoidal lens ($x^2/a^2 + y^2/a^2 + z^2/b^2 = 1$) is chosen, with $a = b\sqrt{(\varepsilon_r - 1)/\varepsilon_r}$, where a, b are the minor and major axes of the ellipsoidal lens, respectively, as shown in Fig. 1. However, the extension length beyond the major axis b is cylindrical instead of elliptical to facilitate the machining process. According to geometrical optics, the length of the cylindrical extension layer L should be equal to $b/\sqrt{\varepsilon_r}$ in order to generate parallel rays through the lens when the feed antenna is located on axis at the far focal point of the ellipsoidal lens. The radiating element used to feed the lens is realized by a single-feed aperture-coupled CP patch antenna (Fig. 1).

The feedline of the antenna is built on a high-permittivity substrate RT/Duroid 6006 ($\varepsilon_r = 6.15$) and the patch antenna is printed on a low-permittivity substrate RT/Duroid 5870 ($\varepsilon_r = 2.33$), which is close to the permittivity of the Rexolite lens. These choices for the substrate are made to increase the bandwidth, as well as to reduce the parasitic radiation losses due to the feed network. The circular polarization is realized by means of a cross-shaped slot in the ground plane, which excites two orthogonal modes in the nearly square patch [19]. The main advantage of this aperture-coupled patch antenna is that the feeding network and the radiating element are well separated by a ground plane and, thus, the patterns are immune to parasitic radiation [7]–[9]. Also, the ground plane yields an increased front-to-back (F/B) ratio, which is important since low-permittivity materials are used. Another advantage is that the single line feed structure is well suited for IC applications. In addition, the cross aperture-coupled structure was reported to yield a significant improvement to CP bandwidth [19]. Finally, it was found through simulations that the circular polarization properties of the structure are not very sensitive to manufacturing tolerances. The cross-slot coupled antenna is designed using HP Momentum, with the lens modeled as an infinite half-space of dielectric constant $\varepsilon_r = 2.54$ [3], [4]. The radiation patterns through the ellipsoidal lens are computed using a geometrical-optics/diffraction theory approach [16], [17]. For this purpose, the following cavity model is utilized to generate the feed patterns for the lens:

$$
\begin{aligned}
E_\theta = &\cos Y \frac{\sin X}{X} \frac{\sin Z}{Z} \sin \phi \\
&+ j \cos X \frac{\sin Y}{Y} \frac{\sin Z}{Z} \cos \phi
\end{aligned}
\tag{1a}
$$

$$
\begin{aligned}
E_\phi = &\cos Y \frac{\sin X}{X} \frac{\sin Z}{Z} \cos \theta \cos \phi \\
&- j \cos X \frac{\sin Y}{Y} \frac{\sin Z}{Z} \cos \theta \sin \phi
\end{aligned}
\tag{1b}
$$

with

$$
X = \frac{k_d L_P}{2} \sin \theta \cos \phi
\tag{2a}
$$

$$
Y = \frac{k_d L_P}{2} \sin \theta \sin \phi
\tag{2b}
$$

$$
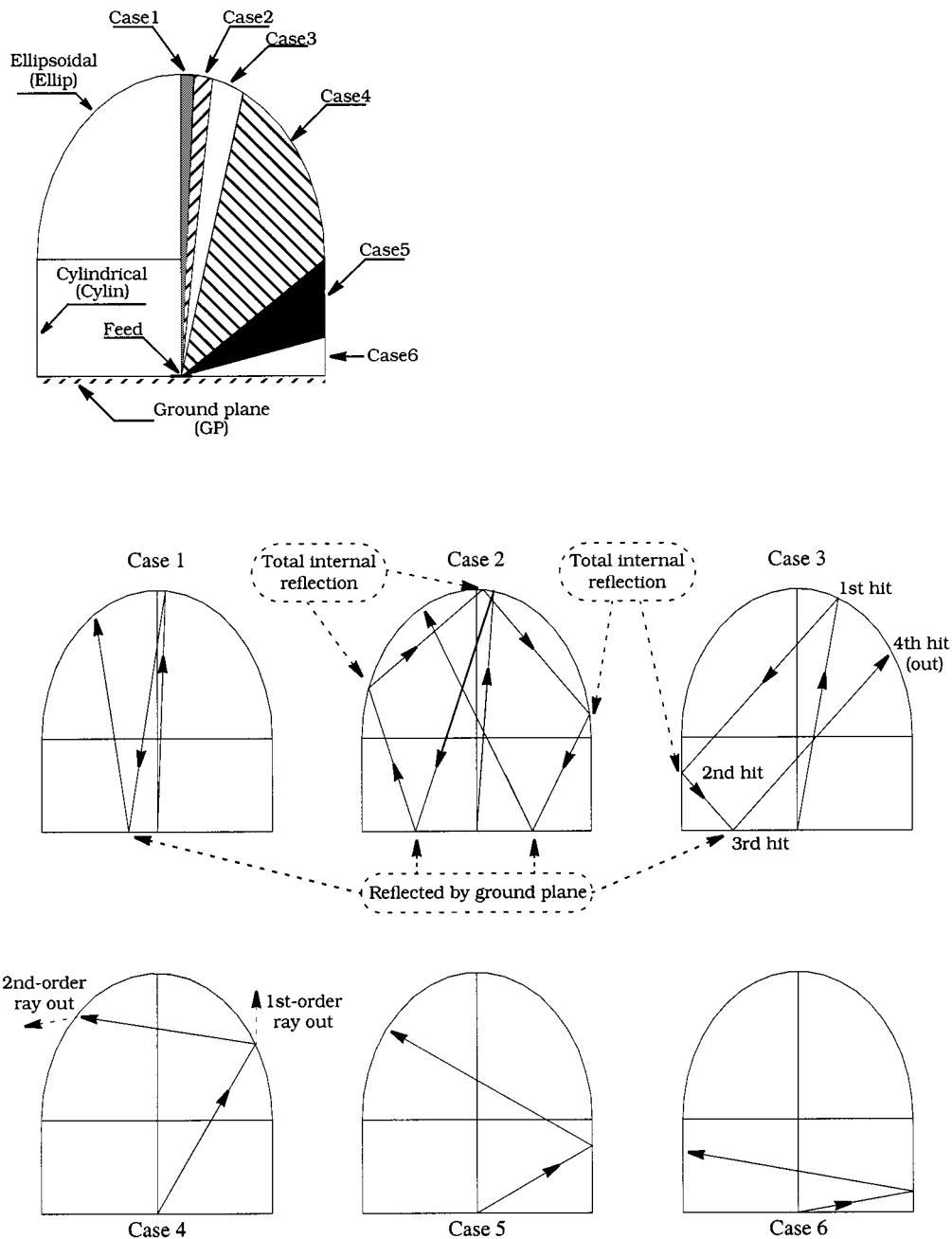Z = \frac{k_d h}{2} \cos \theta
\tag{2c}
$$

Fig. 2. Second-order ray-tracing of reflected waves inside the lens.

where k_d is the wavenumber for the intrinsic lens dielectric, h is the thickness of the patch substrate, and L is the length of the patch. Circular polarization is modeled by introducing a quadrature component (imaginary part) together with the in-phase component (real part). In the literature [15]–[17], reflections at the lens/air interface were only characterized as reflection loss and have not been taken into account for the prediction of the radiation patterns. For a silicon lens ($\varepsilon_r = 11.7$) without a matching layer, a typical reflection loss of 1.5 dB is reported in [15], which implies that 30% of the power is reflected at the lens/air interface. In fact, these reflected rays are not lost, they eventually come out of the lens after multiple reflections inside the lens, reducing the directivity and contributing to the final radiation pattern. Fig. 2 shows

second-order ray-tracing of reflected waves inside the designed lens. In this work, second-order analysis is defined so that a ray is traced after it hits the lens surface for the first time and until it reemerges for a second time. For this analysis, the entire lens surface, including the ellipsoidal lens surface and cylindrical extension layer, can be divided into six different regions, each region corresponding to a different multiple reflection path. Table I lists the corresponding source elevation angle for each region and its trace points on the lens/air interface before the ray exits the lens. For example, Case 1 represents rays with source elevation angles between $0°$ and $2.65°$ and having all trace points for the first hit lying on the ellipsoidal surface. The transmitted waves are accounted for in the first-order ray-tracing, as reported in [15]–[17], and the reflected waves

TABLE I
RAY-TRACING OF REFLECTION WAVES FOR DIFFERENT REGIONS

Case	Source elevation	1st hit	2nd hit	3rd hit	4th hit
1	0°~2.65°	Ellip	GP	Ellip	(out)
2	2.65°~6.15°	Ellip	GP	Ellip	Ellip
3	6.15°~7.5°	Ellip	GP	Cylin	Ellip
	7.5°~12.5°		Cylin	GP	(out)
4	12.5°~51.1°	Ellip	Ellip	(out)	-
5	51.1°~75.0°	Cylin	Ellip	(out)	-
6	75.0°~90°	Cylin	Cylin	(out)	-

continue traveling inside the lens. The trace points for the second hit lie on the ground plane where the rays get totally reflected. Finally, the rays hit the lens boundary for the third time on the ellipsoidal surface and they exit out of the lens. Other cases are similar to Case 1, except Case 2 for which the rays suffer multiple total internal reflections (5~10 times) before finding their way out of the lens.

From the point-of-view of ray tracing, the effect of the lens can be understood in terms of the culmination of the wavefronts emanating from the feeding patch antenna. In this framework, the relationship between the F/B ratio of the substrate lens in terms of the lens antenna directivity and the corresponding properties of the feed patch can be derived as follows. According to the definition, the F/B ratio of the patch and lens antennas, $(F/B)_p$ and $(F/B)_l$, respectively, can be written as

$$(F/B)_p = U_p^f / U_p^b \quad \text{(in the dielectric half-space)} \tag{3a}$$

$$(F/B)_l = U_l^f / U_l^b \quad \text{(in air)} \tag{3b}$$

where U represents the maximum forward or backward radiation intensity of the patch or lens antenna. Furthermore, superscripts f, b represent forward and backward radiation, whereas subscripts p, l represent the patch and lens, respectively. The ratio between the F/B ratios and directivities for the patch and lens antennas can be calculated as

$$\frac{(F/B)_p}{D_p} = \frac{U_p^f / U_p^b}{4\pi U_p^f / P_{\text{in}}} = \frac{P_{\text{in}}}{4\pi U_p^b} \tag{4a}$$

$$\frac{(F/B)_l}{D_l} = \frac{U_l^f / U_l^b}{4\pi U_l^f / P_{\text{in}}} = \frac{P_{\text{in}}}{4\pi U_l^b} \tag{4b}$$

where D_p, D_l are the directivities of the patch and lens antenna, respectively, and P_{in} is the common input power to the patch and lens. We now assume that the back radiation of the patch antenna is not significantly affected when replacing the infinite dielectric half-space above the patch by a finite ellipsoidal lens with the same dielectric constant. This is a reasonable approximation since the lens is electrically large (4~5 free-space wavelengths) and the ground plane provides good isolation between the front and back radiation. From (4a) and (4b), and with $U_p^b \approx U_l^b$, we obtain

$$\frac{(F/B)_p}{D_p} = \frac{(F/B)_l}{D_l}. \tag{5}$$
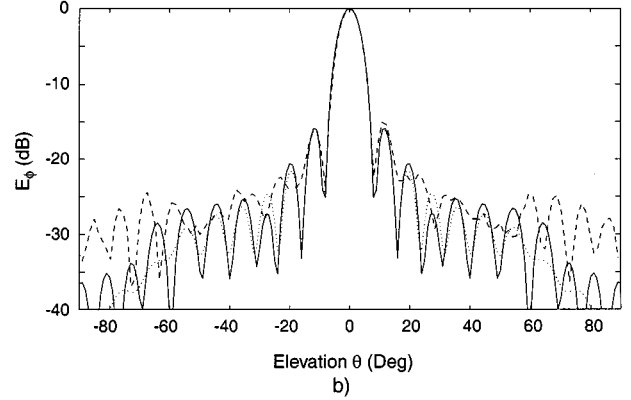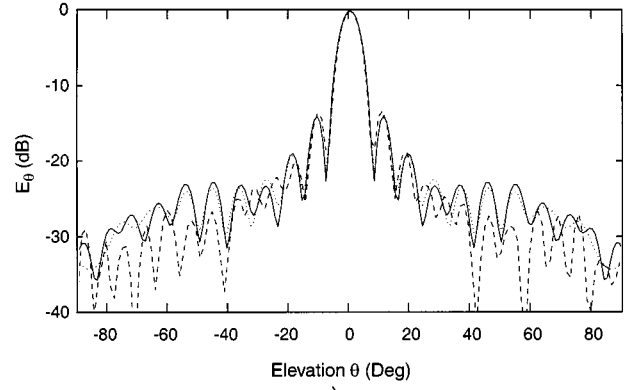
Fig. 3.   Comparison between measured and simulated radiation patterns along the $\phi = 90°$ cut at 30 GHz.

Equation (5) can be rewritten in decibels as

$$\left(\frac{F}{B}\right)_l \approx \left(\frac{F}{B}\right)_p + (D_l - D_p) \quad \text{in dB.} \tag{6}$$

III. SINGLE-BEAM ANTENNA

The previously described lens antenna has been manufactured and characterized experimentally. The measured and calculated radiation patterns for the two orthogonal electric field components E_θ and E_ϕ along the $\phi = 90°$ cut at 30 GHz are shown in Fig. 3. The pattern along the $\phi = 0°$ cut demonstrates a similar behavior. These patterns have been measured in the 6.5 m × 3.5 m × 3.0 m anechoic chamber of the University of Toronto, Toronto, ON, Canada. The antenna under test (lens) and the transmitting *linearly* polarized standard gain horn have been separated by a distance of 4.5 m. The test antenna resides on a rotating pedestal controlled by an Orbit AL-4802-3A positioner. A dedicated Wiltron 360B network analyzer is used for both magnitude and phase pattern measurements to 40 GHz. The dotted line in Fig. 3 represents the simulation with first-order ray tracing only and the solid line corresponds to the total contributions from both first-order ray-tracing and second-order multiple reflections. As shown in Fig. 3, the measurements and simulations agree quite well
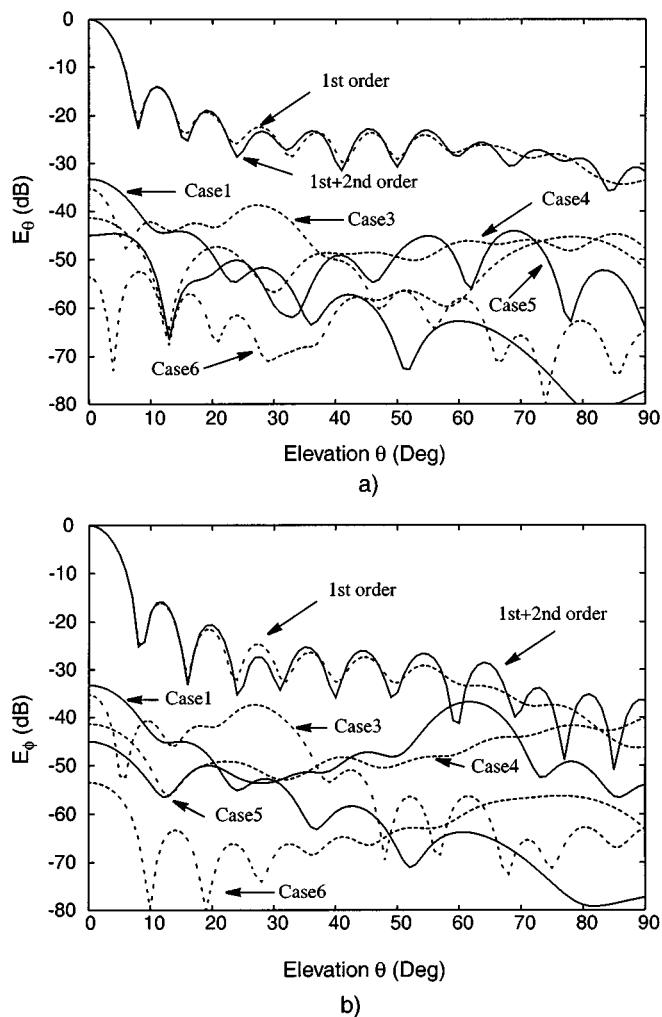
Fig. 4. Contributions of second-order reflected waves to the far-field patterns.

TABLE II
MEASURED AND SIMULATED 3-dB FULL-BEAMWIDTH AND FIRST SIDELOBE
LEVEL FOR $\phi = 90°$ CUT

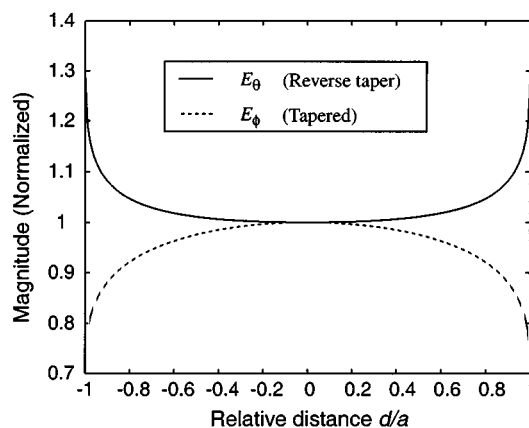|	3 dB full-beamwidth		first sidelobe level	
	measurement	simulation	measurement	simulation
E_θ	6.4°	6.7°	-13.5 dB	-14.0 dB
E_ϕ	6.8°	7.1°	-15.5 dB	-16.0 dB

Fig. 5. Magnitude distributions of the E_θ and E_ϕ components along the $\phi = 90°$ cut over a circular aperture of radius $a = 38.9$ mm in front of the lens.

within the main lobe, first sidelobe, as well as the second sidelobe. According to the simulations, the second-order reflection waves are quite small compared with the first-order ray-tracing and contribute mainly to high-order sidelobes. Fig. 4 shows simulation results for each case defined in Fig. 2. As shown in Fig. 4, Cases 1 and 3 mainly contribute to low-order sidelobes, Cases 4 and 5 mainly contribute to high-order sidelobes and the contribution from Case 6 is much weaker than the other cases. This is true since Cases 1 and 3 correspond to smaller source elevation angles, whereas Cases 4 and 5 correspond to larger source elevation angles. Case 2 is too complicated to be traced in a simple way. However, an effort has been made to trace a few rays in this region, from which it is found that Case 2 has a similar contribution to Cases 1 and 3, i.e., mainly to lower-order sidelobes. It should be pointed out that Cases 1 and 3 arise due to the presence of the ground plane. Without the ground plane, these waves would have been radiated backward increasing the back radiation. This implies that the introduction of the ground plane enhances the F/B ratio.

Table II lists the measured and simulated 3-dB full-beamwidth and first sidelobe level for the E_θ and E_ϕ components. From Table II, it is observed that the E_θ component has a slightly smaller beamwidth and a higher first sidelobe level

than the E_ϕ component. This can be explained by examining the field distribution on an effective circular radiating aperture in front of the lens. The equivalent current distributions on this circular aperture can be determined by a ray-tracing technique. Since the off-axis transmission coefficient for the E_θ component (parallel polarization) through the lens/air interface is greater than the one for the E_ϕ component (perpendicular polarization) and the E_ϕ component vanishes over the patch ground plane, the resulting current distribution for the E_θ component exhibits a reverse tapering while the E_ϕ component exhibits a positive one, as shown in Fig. 5. On the other hand, since the far-field pattern is the Fourier transform of the aperture fields, it is implied that a current distribution with a reverse tapering generates a pattern with smaller beamwidth and higher first sidelobe level than the tapered one. This explains why the E_θ component has a smaller beamwidth and a higher first sidelobe level than the E_ϕ component. In addition, due to this taper of the E_ϕ field, the resulting high-order sidelobes arising from first-order ray tracing are lower than those of the E_θ component. This makes the contribution from second-order reflections comparable to the effect of first-order ray tracing for wide elevation angles [see Figs. 3(b) and 4(b)]. As a result, the high-order sidelobes in the final pattern of the E_ϕ component become higher than what first-order ray-tracing predicts, a trend that is also experimentally observed in Fig. 3(b). Fig. 6 shows the measured and calculated phase for the E_θ and E_ϕ components along the $\phi = 90°$ cut (see Fig. 1) at 30 GHz. The measurements and simulations agree quite well within the entire main lobe. The property of flat phase within the main lobe indicates that diffraction limited patterns have been
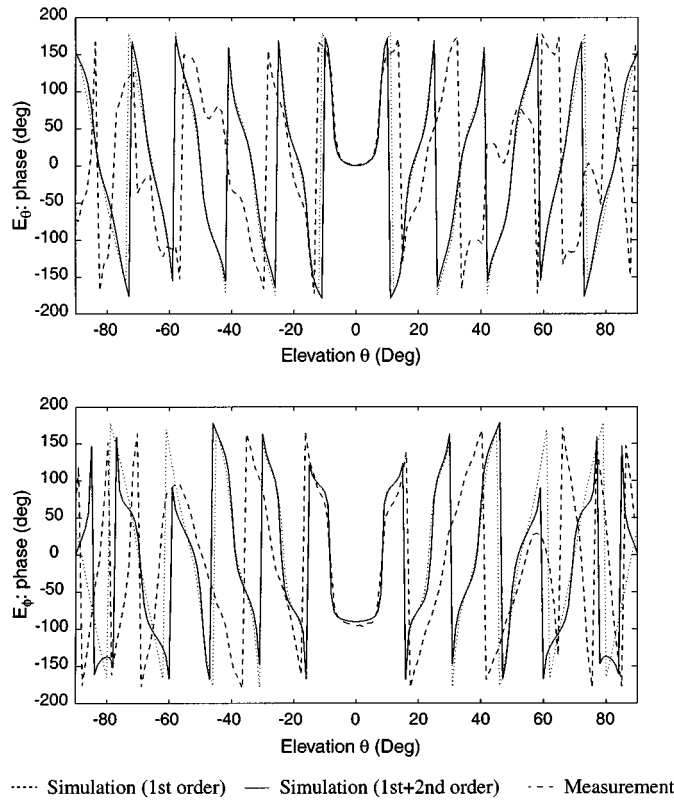
---- Simulation (1st order)   — Simulation (1st+2nd order)   - - - Measurement

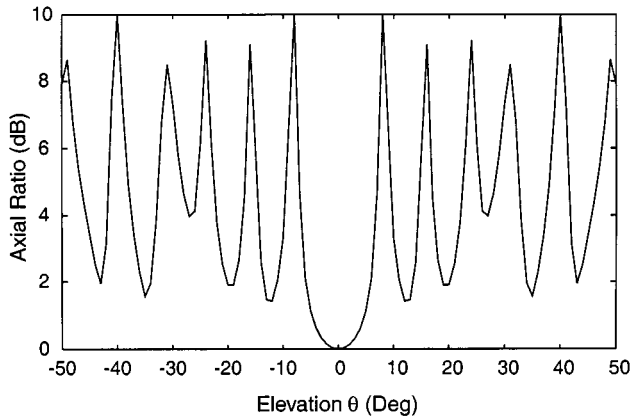Fig. 6.   Phase patterns along the $\phi = 90°$ cut at 30 GHz.

Fig. 7.   Calculated AR as a function of the elevation angle.

achieved. As shown in Fig. 6, there is a $97°$ phase difference between the two measured orthogonal field components at broadside.

Fig. 7 shows the calculated AR as a function of elevation angle, which indicates that the CP through the lens is unaffected at broadside and a good AR is maintained within the main lobe (as small as 0.5 dB within the 3-dB full beamwidth of $7.1°$). At first, this may seem surprising, given that the reflection coefficients for the E_θ and E_ϕ components are, in general, different over the lens surface. However, this rather fortunate result is due to the rotational symmetry of the lens and the fact that along any circular boundary parallel to the x–y-plane (see Fig. 1), the
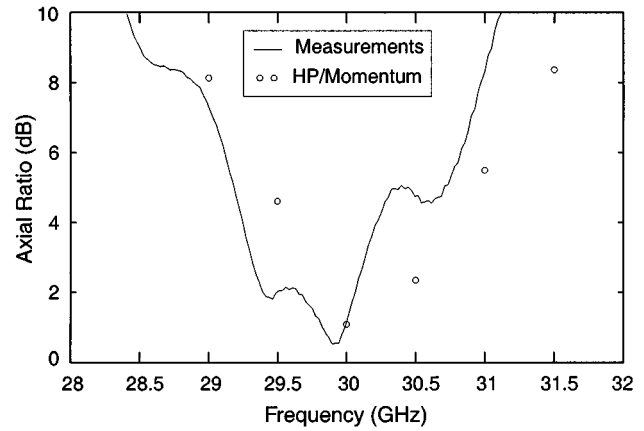

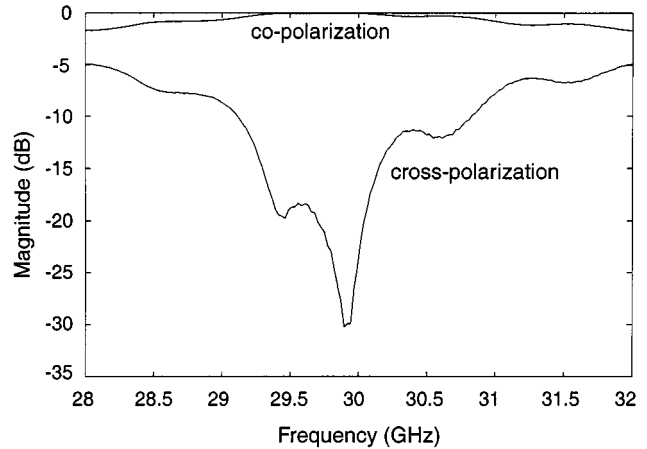Fig. 8.   Measured and simulated AR as a function of frequency.

Fig. 9.   Measured co-polarization (left-hand side) and cross-polarization (right-hand side).

corresponding perpendicular and parallel polarization transmission coefficients, although unequal, are constant. Therefore, the vector integrals of the perpendicular and parallel polarization electric-field components along any circular boundary parallel to the x–y-plane contribute a perfect CP to the on-axis far-field pattern. As a result, ideally the lens antenna exhibits an AR value of 0 dB on axis. The imperfect CP for off-axis positions is introduced by the different taper characteristics of the E_θ and E_ϕ components (see Fig. 5). Fig. 8 shows the measured and simulated broadside AR values as a function of frequency. The AR was constructed from the measured magnitude and phase of the linear components E_θ and E_ϕ. On the other hand, for the simulations, HP Momentum was used to predict the feed patterns rather than the cavity model. Since the lens introduces zero depolarization at broadside, the imperfections of the AR in Fig. 8 are only due to the nonideal feed patch. The best AR of 0.5 dB is achieved around 29.9 GHz and the corresponding 3-dB AR bandwidth is 2.6%. The corresponding decomposition into co- (left-hand side) and cross-polarization (right-hand side) components at broadside as a function of frequency is shown in Fig. 9. These patterns have also been constructed from the corresponding measured magnitude and phase of the linear components E_θ and E_ϕ.

A gain of 23.4±0.2 dB at 30 GHz was measured by the comparison method with a standard gain horn. The indicated ±0.2-dB experimental error is estimated from a consideration of two error sources: 1) reflections in cables and transitions and 2) ambiguity in the standard gain horn calibration curve provided by the manufacturer. On the other hand, the estimated directivity as computed from a far-field integration of the measured fields is 25.9±0.3 dB. The indicated error arises from the involved numerical integration on a finite set of measured sample pattern points. The corresponding loss factor can then be estimated as being equal to 25.9±0.3 dB − 23.4±0.2 dB = 2.5±0.5 dB. This loss can be decomposed in 1.0-dB transmission-line loss, 0.5-dB mismatch loss, 0.5-dB lens absorption, as well as 0.5-dB ohmic/dielectric loss on the patch itself. The ohmic/dielectric efficiency of the patch has been calculated from [21] to be ∼90%. The apparently higher efficiency than what is expected from comparable conventional patches at the same frequency arises from the effectively infinite superstrate (lens) which: 1) eliminates surface-wave losses, thus increasing the efficiency by a factor of ∼1.12 compared to a similar patch printed on a thin ($h/\lambda_0 \approx 0.03$) dielectric substrate and 2) reduces the radiation resistance of the patch by a factor of about $1/\sqrt{\varepsilon_r}$. This, in its turn, lowers the quality factor due to radiation Q_{rad}, thus *dominating* the total quality factor Q_t, resulting in a higher than expected efficiency $\eta = Q_t/Q_{\text{rad}}$. On the other hand, the 1.0-dB transmission-line loss has been computed using HP Momentum and cross verified with Sonnet, and corresponds to about 3.9-cm-long microstrip lines running from the patch antennas to the rim of the lens where they are terminated to K connectors for testing purposes. Therefore, the estimated loss amounts to 1.0 dB + 0.5 dB + 0.5 dB + 0.5 dB = 2.5 dB, which is well within the experimental range of the measured 2.5±0.5 dB loss. Note that the error arising from the ambiguity in exactly detecting the peak of the lens radiation pattern has not been included because it is cancelled out when taking the difference between the *measured* gain and directivity.

The measured directivity of 25.9 dB corresponds to an aperture efficiency of $\eta_1 = 65\%$. This aperture efficiency corresponds to 87% forward coupling efficiency (i.e., neglecting reflections), 18% degradation due to multiple reflections, and 9% back-radiation loss making up a total $\eta_1 = (0.87)(1-0.18)(1-0.09) = 65\%$ aperture efficiency. Furthermore, the measured F/B ratio at 30 GHz is 30 dB, while the simulated F/B ratio of the feed patch antenna from HP Momentum is about 14 dB and the isolated patch directivity is computed to be 7.4 dB. Therefore, the estimated F/B ratio from (6), including 0.5-dB lens absorption loss, is $25.9-0.5-7.4+14 = 32$ dB, which is close to the measured 30-dB F/B ratio of the lens. The 2-dB discrepancy can be attributed to the finite ground plane and the presence of the mounting structure at the back of the lens, which seem to increase the back radiation beyond the original level of the isolated patch radiating in an infinite dielectric half-space.

A very convenient and elegant way of computing the lens system directivity D was implemented through the simple formula $D = 4\pi U_l^f/P_{\text{in}}$, where U_l^f is the on-axis maximum radiation intensity through the lens, as computed from the
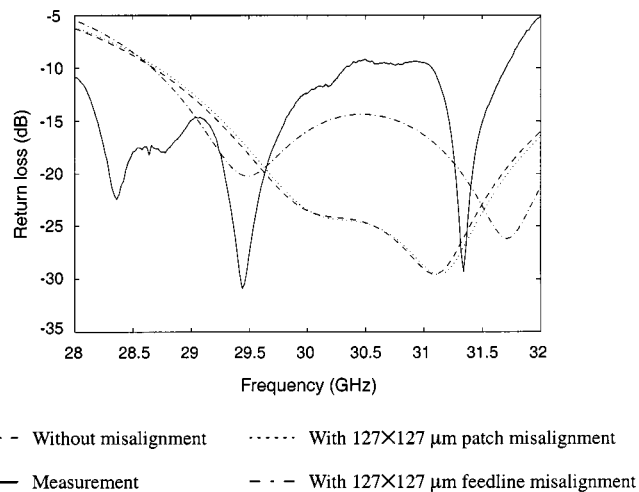

- - - Without misalignment ⋯⋯ With 127×127 μm patch misalignment

—— Measurement – · – With 127×127 μm feedline misalignment

Fig. 10.   Comparison between measured and simulated return loss.

ray-tracing/diffraction approach, and P_{in} is the feed power, as computed by integrating the cavity model fields of the patch inside the dielectric lens. In this formula, reflection losses are automatically accounted for in the directivity. It should be pointed out that reflection losses should not be accounted for in the gain, but in the directivity. This is due to the simple fact that reflected rays eventually reemerge from the lens and contribute to increased sidelobes and lower directivity. Using this approach, the computed directivity amounts to 25.3 dB, which agrees very well with the 25.9 dB estimated from measurements. If reflections were not accounted for in calculating the directivity, then with a forward efficiency of 87%, the directivity would have been $D = 27.0$ dB instead of the measured 25.9 dB. This indicates that there is a 1.1-dB degradation to the directivity due to reflections.

Fig. 10 shows the measured return loss of the feed patch antenna, using an HP8722C vector network analyzer, compared with simulation results. The air gaps between substrates due to the metallization thickness are included in the simulations. The dash line corresponds to the nominal case, which includes two 17-μm-thick air gaps, one between the lens and the patch substrate and another between the feedline and patch substrates. The air gaps can be minimized by tightly assembling the lens antenna. However, physical misalignment between printed layers is more difficult to control. For the structure of Fig. 1, there are two sources of misalignment, namely, patch and feedline misalignment with reference to the center of the cross slots. In Fig. 10, the dotted line and dash–dotted line represent the simulation results, which include an additional 127 × 127 μm patch misalignment and feedline misalignment, respectively. As shown, the input impedance is much more sensitive to the feedline misalignment than to the patch one. The simulations and measurements (solid line) agree better after including an additional feedline misalignment. The residual discrepancy between theory and measurement in Fig. 10 may be attributed to the exact misalignment pattern, which can only be guessed (in Fig. 10 only square patterns are considered), and to second-order reflections from the lens surface, the effect of which becomes nonnegligible for ellipsoidal lenses [5].
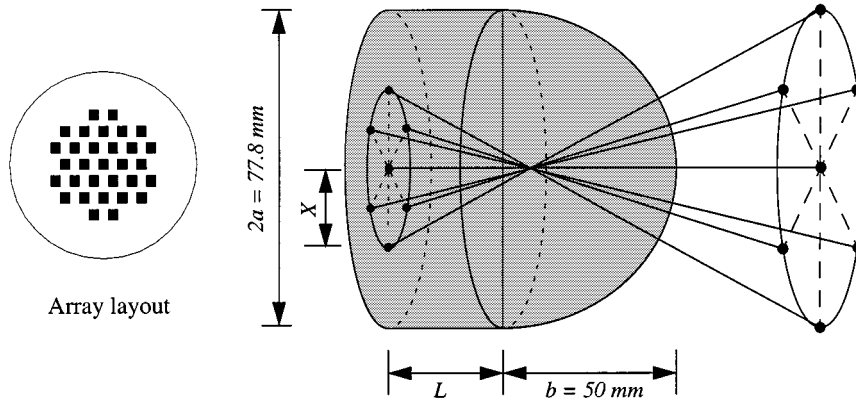
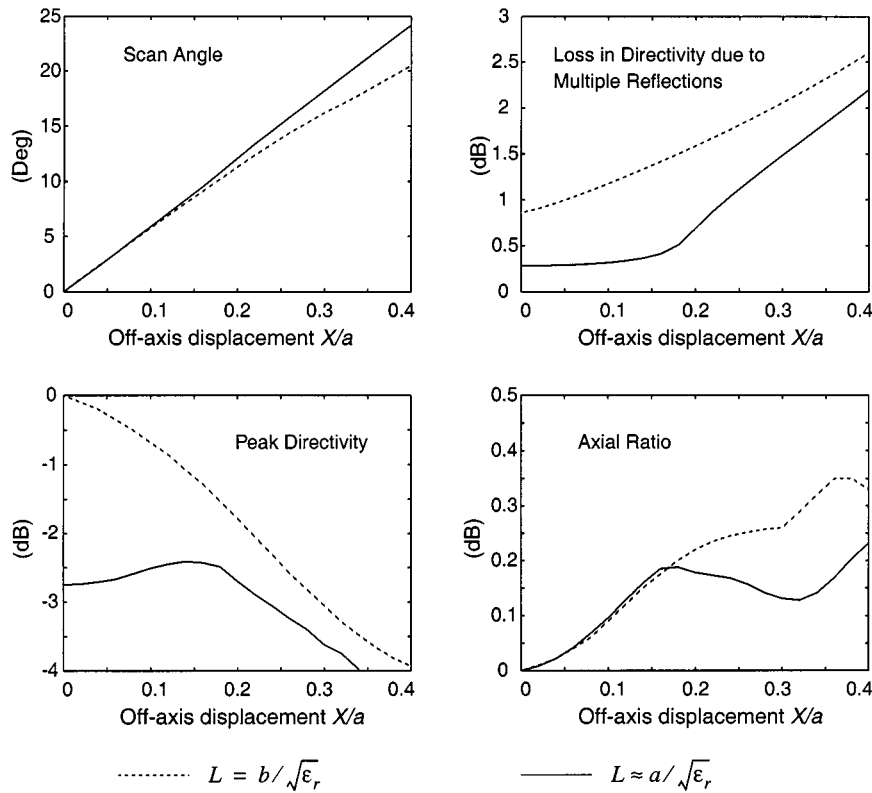Fig. 11.   Multiple-beam launching through substrate lens antenna.

Fig. 12.   Comparison of off-axis scan characteristics (lens radius $a = 38.9$ mm, $b = 50$ mm, $\varepsilon_r = 2.54$, $f = 30$ GHz).

IV. MULTIPLE-BEAM ANTENNA

A. Design

The lens antenna can be used to launch multiple beams by printing an array at the back of the lens [8], [14], [15], as shown in Fig. 11. As shown, a honeycomb patch array at the back of the lens has been chosen as will be discussed below. The scan angle depends on the off-axis displacement X/a, where X is the off-axis distance, and a is the minor axis of the designed ellipsoidal lens. For wireless communications, one of the most important features for multiple-beam antennas is scan coverage. As demonstrated in [15], the off-axis total internal reflection loss is the limiting factor in the design of larger multiple-beam arrays on substrate lenses. For the present CP design, another possible limitation is off-axis depolarization.

As shown in Fig. 12, the peak directivity drops quickly as off-axis displacement increases. In order to launch beams with equal radiation power density and reduce reflection losses, the effect of the extension length L has been numerically investigated and the optimum position has been found to lie around $L \approx a/\sqrt{\varepsilon_r}$. This seems to correspond to the "intermediate" position previously observed for extended hyperhemispherical lenses [15], [16]. Fig. 12 shows the comparison of the simulated scan angle, loss in directivity due to multiple reflections, and peak directivity, as well as the AR as a function of the off-axis displacement X/a between the ellipsoidal lens with extension length $L \approx b/\sqrt{\varepsilon_r}$ and the one with the shorter extension length $L \approx a/\sqrt{\varepsilon_r}$. As shown, the peak directivity of the lens becomes much flatter with the smaller extension length. However, this is accompanied by a penalty of 2.7-dB reduction
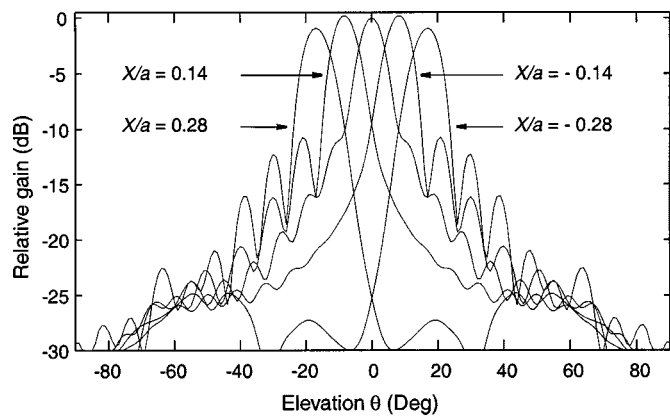
Fig. 13. Off-axis radiation patterns for a linear array of patches along the x-axis, $L \approx a/\sqrt{\varepsilon_r} = 24.4$ mm.
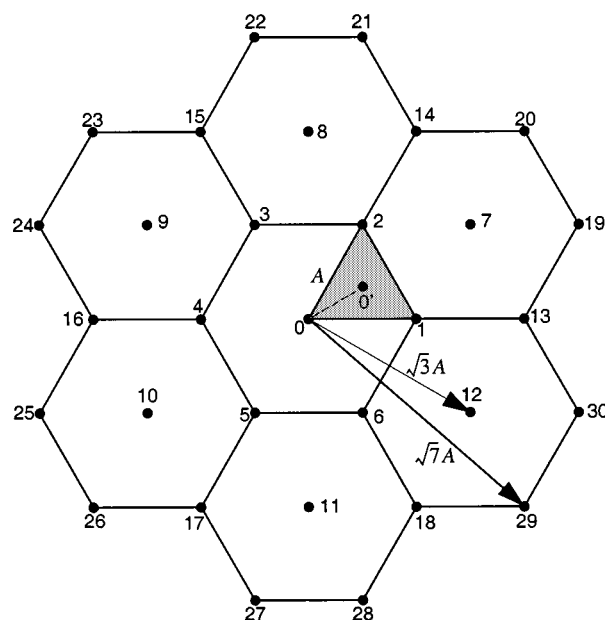

Fig. 14. Hexagonal arrangement of the antenna patch array at the back of the lens.

TABLE III
RELATIVE DIRECTIVITY AND OVERLAPPING LEVEL IN SHADED
EQUILATERAL TRIANGLE OF FIG. 14

Beam	Relative Directivity (dB)	Overlapping Beams	Overlapping level (dB)
#0	0	#0∩#1(#2)	-2.0
#1	+0.2	#1∩#2	-2.0
#2	+0.2	#0∩#1∩#2	-2.7

of the on-axis directivity. The scan angle and the loss in directivity are also better with the shorter extension length, an observation that is consistent with the case of an extended hemispherical lens in [15]. For the ellipsoidal lens with the shorter extension length $L \approx a/\sqrt{\varepsilon_r}$, the loss in directivity is only 0.3 dB on axis and increases rapidly after off-axis displacements of $X/a = 0.16$. The loss in directivity remains smaller than 1.8 dB for a maximum off-axis displacement of $X/a = 0.34$. On the other hand, the corresponding AR exhibits a value of 0 dB on axis and remains smaller than 0.25 dB within an off-axis displacement of $X/a = 0.40$. This indicates that the induced depolarization for off-axis cases is fairly small and can be neglected. From the above discussion, it can be concluded that the designed lens structure can be used up to off-axis displacements of $X/a = 0.34$, resulting in a maximum loss in directivity of 1.8 dB due to multiple reflections, which corresponds to a scan angle of $\pm 20°$ (i.e., a total of $40°$).

Once the maximum allowed off-axis displacement $X/a = 0.34$ has been determined based on the maximum tolerable loss in directivity, the array at the back of the lens can be designed. First, a linear array has been designed with beams that overlap at a 3-dB level, with the corresponding simulated radiation patterns shown in Fig. 13. To achieve the 3-dB beam overlapping for the linear array, the distance between adjacent elements $d_{3\,dB}$ has been determined to be $0.14a$. Note that the patterns are fairly circularly symmetric and, therefore, this interelement distance of $d_{3\,dB}$ ensures a 3-dB beam overlapping in any azimuthal cut plane. Next, a planar array has been designed and implemented based on a hexagonal arrangement of the patches at the back of the lens for maximizing scan coverage with a minimum number of array elements (see Fig. 11). The distance between neighboring elements A in Fig. 14 should be optimized based on the beamwidth of adjacent beams and the required beam overlapping level (e.g., 3 dB). The maximum radius of this hexagonal array is limited by the allowed off-axis displacement of $0.34a$ in this case. For the shaded equilateral triangle of Fig. 14, the point of minimum overlapping power among beams 0, 1, and 2 occurs at the center of the triangle (point O'). In order to get 3-dB beam overlapping at point O', the distance $\overline{OO'}$ should be equal to $d_{3\,dB} = 0.07a$. The distance between neighbor elements A can then be determined as equal to $\sqrt{3} \times \overline{OO'} \approx 0.12a$. As

shown in Fig. 14, the allowed largest off-axis displacement is, therefore, $\sqrt{7}A \approx 0.32a$. The hexagon array launches 31 beams and achieves a 3-dB scan coverage of $45.4°$. Table III lists a summary of beam overlapping levels within the shaded triangular area of Fig. 14. The first two overlapping levels of Table III refer to the midpoints of the sides of the equilateral triangle, while the third refers to its center. As indicated, the lowest beam coupling level is -2.7 dB at the center of the shaded triangle point O' in Fig. 14. Since the peak directivity has been optimized not to vary drastically with distance, the same design procedure can be extended to the remaining triangles in Fig. 14, ensuring a 3-dB coupling level for all adjacent beams.

B. Experimental Results

The previously described multiple-beam lens antenna has been implemented at the nominal design frequency of 30 GHz. Fig. 15 shows the measured and simulated E_θ patterns for four representative patch elements at 30.4 GHz. Each patch corresponds to different off-axis displacements X/a of 0, 0.12, 0.24, and 0.32, respectively. The measurements and simulations agree quite well within the main lobe and the peak positions of the off-axis beams have been exactly predicted. This is also true for the measured and simulated phase patterns, which
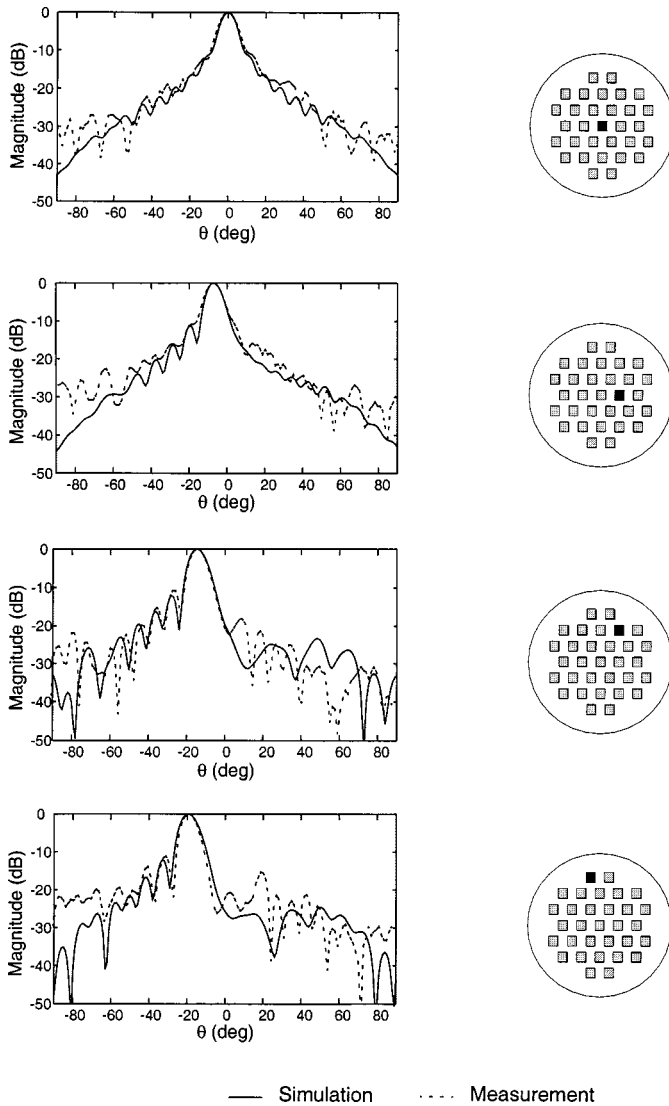
Fig. 15. Multiple-beam patterns at $f = 30.4$ GHz.

Fig. 16. Comparison between measured and simulated AR for the multiple-beam antenna.

are not shown here for brevity. In addition, the measured E_ϕ magnitude and phase patterns exhibit similar behavior, but are also not shown here due to space limitations. It should be noted that the operating frequency has been found slightly shifted from the nominal 30 to 30.4 GHz. This becomes more apparent when examining the measured AR for the selected patches shown in Fig. 16 compared to HP Momentum simulations for an isolated patch radiating into an infinite dielectric half-space with $\varepsilon_r = 2.54$. In all likelihood, this frequency shift is due to mutual coupling effects, which have not been taken into account for designing the hexagonal patch array. Nevertheless, as shown in Fig. 16 at 30.4 GHz, all patches exhibit an AR, which is smaller than 2 dB, a level that should be adequate for most applications. Furthermore, the measured isolation between adjacent patches is typically -30 dB at 30.4 GHz and does not exceed the level of -26 dB in the frequency range of 28–32 GHz. It should be pointed out that these isolation results include mutual coupling effects between the interconnecting microstrip transmission lines that connect the patches to K connectors at the rim of the lens. In addition, the measured gain
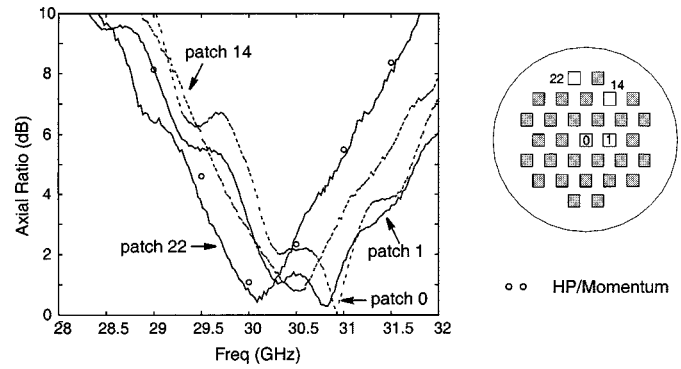
variation for each element across the array in the frequency range of 28–32 GHz does not exceed 1.5 dB.

V. CONCLUSIONS

A single- and multiple-beam CP ellipsoidal type of substrate lens antennas suitable for future broad-band mm-wave wireless communications have been designed, implemented using Rexolite, and experimentally characterized. For this purpose, a comprehensive design procedure has been introduced.

The single-beam lens antenna exhibits clean axially symmetric patterns, a directivity of 25.9 ± 0.3 dB, a F/B ratio of 30 dB, and a 3-dB pattern full-beamwidth of $6.6°$ at 30 GHz. It is found and explicitly explained that circular polarization through the ellipsoidal lens is maintained within the main lobe. The measured AR is about 0.5 dB and the corresponding 3 dB AR bandwidth is 2.6%. In addition, the measured impedance bandwidth is 12.5% within a $SWR \leq 1.8:1$. During the design procedure, the depolarization properties of the lenses have been investigated, the role of multiple internal reflections on the patterns and directivity of the lens has been clarified, and a useful expression for computing the lens F/B ratio has been provided. The presented substrate lens antenna is well suited for mm-wave broad-band point-to-point wireless communications.

The multiple-beam lens antenna has been designed for maximum beam coverage with a minimum number of patch elements. For this purpose, the off-axis characteristics of the ellipsoidal lens have been characterized and a hexagonal array has been chosen and designed. The lens antenna launches 31 beams with a 3-dB minimum overlapping level between adjacent beams and a 3-dB scan coverage of $45.4°$. The effect of mutual coupling among the patch elements has been experimentally characterized and the measured isolation between adjacent patches is typically -30 dB at the design frequency. The multiple-beam lens is well suited for point-to-multipoint indoor applications such as a broad-band wireless local area network (LAN).

REFERENCES

[1] W. Honcharenko, J. P. Kruys, D. Y. Lee, and N. J. Shah, "Broadband wireless access," *IEEE Commun. Mag.*, pp. 20–26, Jan. 1997.

[2] R. Douville, D. Roscoe, M. Cuhaci, and M. Stubbs, "Antennas for broadband microwave/mm-wave communications systems," in *Broadband Wireless Communications*, M. Louise and S. Pupolin, Eds. Berlin, Germany: Springer-Verlag, 1998, pp. 138–148.

[3] G. V. Eleftheriades and G. M. Rebeiz, "Self and mutual admittance of slot antennas on a dielectric half-space," *Int. J. Infrared Millim. Waves*, vol. 14, no. 10, pp. 1925–1946, Oct. 1993.

[4] P. Otero, G. V. Eleftheriades, and J. R. Mosig, "Integrated modified rectangular loop slot antenna on substrate lenses for mm-and sub-mm-wave frequencies mixer applications," *IEEE Trans. Antennas Propagat.*, vol. 46, pp. 1489–1497, Oct. 1998.

[5] A. Neto, S. Maci, and P. J. I. de Maagt, "Reflections inside an elliptical dielectric lens antenna," *Proc. Inst. Elect. Eng.*, vol. 145, no. 3, pp. 243–247, June 1998.

[6] M. J. M. van der Vorst, "Integrated lens antennas for submillimeter-wave applications," Ph.D. dissertation, Dept. Elect. Eng., Tech. Univ. Eindhoven, Eindhoven, The Netherlands, 1999.

[7] G. V. Eleftheriades, Y. Brand, J. Zürcher, and J. R. Mosig, "ALPSS: A millimeter-wave aperture-coupled patch antenna on a substrate lens," *Electron. Lett.*, vol. 33, no. 3, pp. 169–170, Jan. 1997.

[8] K. Uehara, K. Miyashita, K. I. Natsume, K. Hatakeyama, and K. Mizuno, "Lens-coupled imaging arrays for the mm and sub-mm-wave regions," *IEEE Trans. Microwave Theory Tech.*, vol. 40, pp. 806–811, May 1992.

[9] X. Wu, G. V. Eleftheriades, and E. van Deventer, "A mm-wave circularly polarized substrate lens antenna for wireless communications," in *Proc. ANTEM Conf.*, Ottawa, ON, Canada, August 1998, pp. 595–598.

[10] D. B. Rutledge, D. P. Neikirk, and D. Kasilingam, "Integrated circuit antennas," in *Infrared and Millimeter-Waves*, K. J. Button, Ed. New York: Academic, 1983, vol. 10, pp. 1–90.

[11] J. Zmudzinas, "Quasioptical slot antenna SIS mixers," *IEEE Trans. Microwave Theory Tech.*, vol. 40, pp. 1797–1804, Sept. 1992.

[12] S. S. Gearhart and G. M. Rebeiz, "A monolithic 250 GHz Schottky-diode receiver," *IEEE Trans. Microwave Theory Tech.*, vol. 42, pp. 2504–2511, Dec. 1994.

[13] G. V. Eleftheriades, J. Zürcher, and J. R. Mosig, "Pattern and efficiencies of slot-fed mm-wave glass–ceramic substrate lens antennas," in *Proc. ESA/ESTEC Millimeter Wave Tech. Applicat. Workshop*, Noordwijk, The Netherlands, Dec. 1995, pp. 2.2.1–2.3.1.

[14] X. Wu, G. V. Eleftheriades, and E. van Deventer, "Design and characterization of single and multiple beam mm-wave circularly polarized substrate lens antennas for wireless communications," in *Proc. IEEE Int. Antennas Propagat. Symp. Dig.*, Orlando, FL, July 1999, pp. 2408–2411.

[15] D. F. Filipovic, G. P. Gauthier, S. Raman, and G. M. Rebeiz, "Off-axis properties of silicon and quartz dielectric lens antennas," *IEEE Trans. Antennas Propagat.*, vol. 45, pp. 760–766, May 1997.

[16] D. F. Filipovic, S. S. Gearhart, and G. M. Rebeiz, "Double-slot antennas on extended hemispherical and elliptical silicon dielectric lenses," *IEEE Trans Microwave Theory Tech.*, vol. 41, pp. 1738–1749, Oct. 1993.

[17] D. Filipovic, G. V. Eleftheriades, and G. M. Rebeiz, "Off-axis imaging properties of substrate lens antennas," in *5th Int. Space Terahertz Tech. Symp. Dig.*, Ann Arbor, MI, Feb. 1994, pp. 778–787.

[18] J. C. Liberty and T. S. Rappaport, *Smart Antennas for Wireless Communications*. Englewood Cliffs, NJ: Prentice-Hall, 1999.

[19] T. Vlasits, E. Korolkiewicz, A. Sambell, and B. Robinson, "Performance of a cross-aperture coupled single feed circularly polarized patch antenna," *Electron. Lett.*, vol. 32, no. 7, pp. 612–613, Mar. 1996.

[20] P. F. Goldsmith, *Quasioptical System*. Piscataway, NJ: IEEE Press, 1998, p. 82.

[21] C. A. Balanis, *Antenna Theory: Analysis and Design*, 2nd ed. New York: Wiley, 1997, pp. 760–762.

Xidong Wu (S'91) was born in Wuxi, China, in 1970. He received the B.S. degree from Southeast University, Nanjing, China, in 1989, the M.S. degree from the University of Toronto, Toronto, ON, Canada, in 1996, both in electrical engineering, and is currently working toward the Ph.D. degree in electromagnetics at the University of Toronto.

Since 1996, he has been with the Electromagnetic Laboratory, University of Toronto. His current research interests include antennas for wireless communications, numerical electromagnetics, and mm-wave circuits.

George V. Eleftheriades (S'86–M'88) received the Ph.D. and M.S.E.E. degrees in electrical engineering from The University of Michigan at Ann Arbor, in 1993 and 1989, respectively, and the diploma in electrical engineering from the National Technical University of Athens, Athens, Greece, in 1988.

From 1994 to 1997, he was with the Swiss Federal Institute of Technology, Lausanne, Switzerland, where he was engaged in the design of mm-wave and submillimeter-wave receivers and in the creation of fast computer-aided design (CAD) tools for planar packaged microwave circuits. In 1997, he joined the Department of Electrical and Computer Engineering, University of Toronto, Toronto, ON, Canada, as Assistant Professor. He has authored or co-authored over 50 papers in refereed journals and conference proceedings. His current research interests include mm-wave IC antennas and components for broad-band wireless communications, low-loss micromachined components for Ka-band satellite communications and local multipoint distribution service (LMDS), submillimeter-wave receivers for remote sensing, and electromagnetic design for high-speed digital circuits.

Dr. Eleftheriades was a corecipient of the 1990 Best Paper Award presented at the 6th International Symposium on Antennas (JINA), a recipient of a 1992 Student Paper Award presented at the 1992 IEEE Antennas and Propagation Symposium, and the 1991 Distinguished Achievement Award presented by The University of Michigan at Ann Arbor. In August 2000, one of his students won first prize in the Student Competition of the Symposium on "Antenna Technology and Applied Electromagnetics (ANTEM), Winnipeg, MB, Canada.

T. Emilie van Deventer-Perkins (SM'96) received the Diplome Universitaire de Technologie from the Institut Universitaire de Technologie of Marseille, Marseille, France, and the B.S.E, M.S.E. and Ph.D. degrees in electrical engineering from The University of Michigan at Ann Arbor.

She is currently an Associate Professor in the Department of Electrical and Computer Engineering, University of Toronto, Toronto, ON, Canada, where she holds the National Sciences and Engineering research Council of Canada (NSERC)/Bell Canada Junior Industrial Chair in Electromagnetics. Her research interests include the numerical modeling of microwave and mm-wave structures and digital interconnects.

Dr. van Deventer-Perkins is the founder of the IEEE Microwave Theory and Techniques Society (IEEE MTT-S), IEEE Antennas and Propagation Society (IEEE AP-S), and the IEEE Electromagnetic Compatibility (IEEE EMC) Society of the IEEE Toronto Section.